Manuscript Details

Manuscript number	JQSRT_2016_729
Title	Broadband Chemical Species Tomography: Measurement Theory and a Proof-of-Concept Emission Detection Experiment
Article type	Full Length Article

Abstract

This work introduces broadband-absorption based chemical species tomography (CST) as a novel approach to reconstruct hydrocarbon concentrations from open-path attenuation measurements. In contrast to monochromatic CST, which usually involves solving a mathematically ill-posed linear problem, the measurement equations in broadband CST are nonlinear due to the integration of the radiative transfer equation over the detection spectrum. We present a transfer function that relates broadband transmittances to a path-integrated concentration, suitable for tomographic reconstruction, and use a Bayesian reconstruction technique that combines the measurement data with a priori assumptions about the spatial distribution of the target species. The technique is demonstrated by reconstructing a propane plume, and validating the results by point concentration measurements made with a flame ionization detector.

Keywords	emissions detection; fugitive emissions; tomography; broadband tomography; inverse analysis
Corresponding Author	Samuel Grauer
Corresponding Author's Institution	University of Waterloo
Order of Authors	Samuel Grauer, Roger Tsang, Kyle Daun
Suggested reviewers	Jay Jeffries, Scott Sanders, Hugh McCann, Paul Wright

Submission Files Included in this PDF

File Name [File Type]

Response_JQSRT-2016-729.pdf [Response to reviewers]

Revision_SG.pdf [Manuscript]

Highlights_SG.pdf [Highlights]

To view all the submission files, including those not included in the PDF, click on the manuscript title on your EVISE Homepage, then click 'Download zip file'.

Broadband Chemical Species Tomography: Measurement Theory and a Proof-of-Concept Emission Detection Experiment

Samuel J. Grauer,[a,*] Roger W. Tsang,[a] Kyle J. Daun[a]

\

[a]Department of Mechanical and Mechatronics Engineering
University of Waterloo
200 University Avenue West
Waterloo ON Canada, N2L 3G1

*Corresponding author: sgrauer@uwaterloo.ca

Abstract

This work introduces broadband-absorption based chemical species tomography (CST) as a novel approach to reconstruct hydrocarbon concentrations from open-path attenuation measurements. In contrast to monochromatic CST, which usually involves solving a mathematically ill-posed linear problem, the measurement equations in broadband CST are nonlinear due to the integration of the radiative transfer equation over the detection spectrum. We present a transfer function that relates broadband transmittances to a path-integrated concentration, suitable for tomographic reconstruction, and use a Bayesian reconstruction technique that combines the measurement data with *a priori* assumptions about the spatial distribution of the target species. The technique is demonstrated by reconstructing a propane plume, and validating the results by point concentration measurements made with a flame ionization detector.

Keywords

Highlights

- A broadband measurement model is developed for chemical species tomography.
- Transfer functions map broadband transmittances to a path-integrated concentration.
- A system of open-path broadband infrared detectors was constructed and calibrated.
- Target gasses in this study are methane, ethylene, and propane.
- The first broadband CST experiment is reported, featuring a propane plume source.

1   Introduction

The release of fugitive hydrocarbons into the atmosphere poses health and safety hazards [1-3] and contributes to climate change [4]. Most often, emission fluxes from industrial sources are estimated using point concentration measurements (*e.g.*, flame ionization detectors (FIDs) [1,5], catalytic pellistor sensors [6,7], semiconductor sensors [8], and closed-path absorption spectroscopy [9,10]) coupled with empirical emissions factors and mass balance calculations [11,12]. These practices are notoriously unreliable, however, and are limited by the inherent locality of point concentration measurements [13]. Moreover, point-measurement surveys are costly, time-consuming, and often require personnel to work under hazardous conditions.

Such shortcomings motivate the development of stand-off optical methods for quantifying fugitive emissions. Optical methods exploit the fact that hydrocarbons absorb, emit, and scatter radiation at select wavelengths that are transparent to other ambient species. One of the most accurate of these techniques is differential absorption light detection and ranging, DIAL, which infers the concentration of airborne hydrocarbons from the difference between backscattered laser light measured at two wavelengths [14]. DIAL provides highly accurate environmental measurements of volatile organic compounds (VOCs) in the C_2 to C_{22} range, including alkanes, alkenes, aromatics, benzene, and toluene, as well as simple molecules like methane (CH_4) [12,15-20], but is too costly and complex to use on a daily basis.

Open-path (OP) absorption measurements infer the path-integrated concentration of the target species, measuring the intensity attenuated by a gas between a transmitter and receiver. The path-integrated gas molecular concentration is assumed to scale with the average absorption or extinction coefficient *via* the Beer-Lambert law. OP techniques based on tunable diode laser absorption spectroscopy (TDLAS), differential absorption spectroscopy (DOAS), and OP Fourier-transform infrared (OP-FTIR) spectroscopy have been extensively deployed for quantifying fugitive emissions [21,22]. TDLAS measurements are generated by scanning a monochromatic source over a short spectral range. The reference intensity is inferred from wavenumbers that do not correspond to an absorption line. Transmittance data is resolved for multiple lines, which may be used to infer the concentration of multiple species as well as temperature and pressure [23]. DOAS is similar to TDLAS, except it uses ambient solar radiation or a broadband thermal source, which is spectrally-resolved at the detection stage by a scanning monochromator, spectrograph,

prism spectrophotometer, or interferometer (as in FTIR) [24,25]. OP-FTIR is essentially DOAS with a broadband thermal source and interferometer-equipped detector.

Individual OP measurements only provide path-integrated concentration data. Therefore, in order to accurately quantify an emission flux or image and localize a source, multiple measurements must be combined and augmented with assumptions about the target species, resulting in a 2D or 3D concentration map. For instance, in radial plume mapping (RMP) a measurement plane is defined downwind from an emission source, and three or more OP measurements are made across the plane. A presumed Gaussian or bi-Gaussian plume profile is then fit to the measurements to obtain a spatial concentration map, which is combined with anemometry measurements to obtain a flux estimate [26]. Numerous RPM experiments have found the distribution shape to strongly influence the net emission estimate [27-29]; moreover, a source can vary in shape and location over time. As such, it is desirable to relax shape constraints on the gas distribution.

Absorption chemical species tomography (CST) maps the spectral absorption coefficient, in a domain using OP measurements between a transmitter (*i.e.*, a laser, broadband thermal source, or LED) and receiver, without assuming a specific distribution shape [30]. McCann *et al.* [31] and Cai and Kaminski [32] recently reviewed the state-of-the-art in CST. While lab-scale experiments make up the bulk of CST studies, this technique has also been deployed to monitor environmental emissions. For instance, Piper *et al.* [33] used a 16-beam OP-FTIR array to map the concentration of sulfur hexafluoride over a 70×70 m area. Todd *et al.* [34] reconstructed the ammonia distribution over a 107×255 m lagoon with a 17-beam OP-FTIR array. Laepple *et al.* [35] constructed a similar 16-path system from two DOAS telescopes and retro-reflectors, which they used to image the distribution of nitrogen dioxide over a highway in Germany. More recently, UV-DOAS schemes were constructed to image the volcanic emission of sulfur dioxide (SO_2) [36,37]. Rivera *et al.* [38] and Zhang *et al.* [39] applied optical emissions tomography to industrial settings, reconstructing a SO_2 distribution with absorption spectrometers and a CH_4 distribution with a TDLAS system, respectively. The number of optical paths in each of these studies was small due to the high cost of tunable light sources and spectrally-resolved detectors. Increasing the number of paths can dramatically improve the accuracy of reconstructions, however, which motivates the search for an alternative, low-cost approach to spectroscopic tomography.

To the best of the authors' knowledge, CST on molecular gases has exclusively relied on spectrally-resolved absorption lines. (Polychromatic measurements are also spectrally-resolved, *i.e.*, using TDLAS, DOAS, and FTIR devices.) However, broadband transmittance measurements also indicate the path-integrated concentration of an emissions plume *via* low-cost, commercially-available OP detectors. Moreover, many of these devices are intrinsically safe, and can therefore be deployed at industrial facilities without modification. However, broadband transmittances are a nonlinear function of the gas burden. As such, in order to apply CST reconstruction techniques to broadband transmittances, a new procedure is required to process the measurement data.

This work reports the development of such a procedure and the results of the first broadband CST experiment. Broadband transmittances were measured with an incandescent source (a silicon nitride globar) and a photovoltaic detector equipped with a bandpass filter. The filter range was aligned with the main ro-vibrational HC stretching band at 3.3 μm. Bandpass filters omit most incoming radiation but nonetheless combine light over a spectrum that includes many spectral lines, giving rise to the nonlinear dependence of transmittance on path-integrated concentration. We therefore developed a transfer function to account for this spectral convolution, specific to a target species over a set spectral range. Transfer functions were constructed for CH_4, ethylene (C_2H_4), and propane (C_3H_8), over a range corresponding to the bandpass filter window, using a spectral line database [40] and high-resolution spectral transmittance-reference data [41].

The technique is demonstrated by imaging a propane plume, perturbed by advection normal to the flow. Tomographic measurements were made with a 35-path array and linearized with the C_3H_8 transfer function. A Bayesian framework was employed to reconstruct the plume, using a Tikhonov prior to promote spatially-smooth estimates. The reconstructed plume structure agreed with point concentrations made using a flame ionization detector (FID). Our results support the development of broadband CST for the quantification of anisotropic, time-varying hydrocarbon emissions.

2   Broadband Tomography

2.1   Monochromatic absorption tomography

Figure 1 illustrates a monochromatic OP measurement at wavenumber η through an absorbing gas. The measurement model assumes that the field is discretized into pixels that contain a uniform concentration of gas.
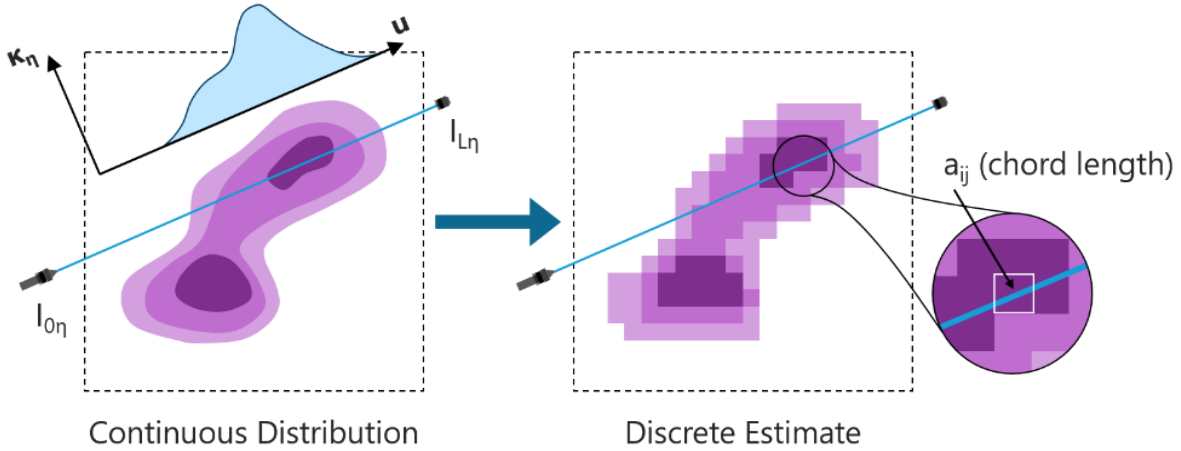

Figure 1: Absorption CST schematic with a single OP measurement and a discrete estimate of the gas distribution. The absorption coefficient relates to properties of interest; the discrete model assumes constant gas properties in each pixel.

The CST measurement model derives from the radiative transfer equation (RTE), which is simplified by neglecting thermal emission and scattering. This results in the Beer-Lambert law

$$I_{L\eta} = I_{0\eta} \exp\left\{-\int_0^L \kappa_\eta\left[\mathbf{r}(u)\right]du\right\}, \tag{1}$$

where $\mathbf{r}(u)$ is a vector function that points at a position along the path corresponding to a parametric distance u between the transmitter ($u = 0$) and the receiver ($u = L$); $I_{0\eta}$ is the spectral intensity of the source; $I_{L\eta}$ is the spectral intensity at the detector; and κ_η is the spectral absorption coefficient, which is proportional to the local target species concentration (discussed further in Section 2.2). Equation (1) is rearranged into a Fredholm integral equation of the first kind (IFK)

$$b_i \equiv \ln\left[\frac{I_{0\eta}}{I_{L\eta}}\right] = \int_0^L \kappa_\eta\left[\mathbf{r}(u)\right]du, \tag{2}$$

where b_i is the path-integrated absorption coefficient along the ith optical path. A total of m paths transect the domain, and the corresponding measurements b_i are arranged to form the vector $\mathbf{b} \in \mathbb{R}^m$.

Distributions of estimated quantities, e.g. species concentration, must be represented in some parametric form. A common choice is to represent the unknown gas concentration using n square pixels [24], as in Figure 1, each of which contains a uniform concentration of the target species. Estimates of κ_η are therefore represented as a vector of coefficients $\mathbf{x} \in \mathbb{R}^n$ and Eq. (2) is approximated by a "ray-sum"

$$b_i \approx \sum_{j=1}^{n} a_{ij} x_j \, , \tag{3}$$

where a_{ij} is the chord length of the ith path in the jth pixel, shown in Figure 1. Collectively, the ray-sums for each path yield the ray-sum matrix $\mathbf{A} \in \mathbb{R}^{m \times n}$, resulting in the matrix equation $\mathbf{Ax} = \mathbf{b}$. In most CST experiments the number of paths m is limited due to equipment costs and restrictions on optical access. If the uniform pixel concentration assumption is to be reasonable, pixels must be small so n, in turn, will be large. Under those circumstances, $m < n$ and the system is rank-deficient, according to the rank-nullity theorem. In other words, since there are more variables than equations, an infinite set of $\mathbf{x}$ vectors will satisfy any measurement vector $\mathbf{b}$. As such, *a priori* information must be added to the measurement data to estimate $\mathbf{x}$.

Bayesian tomography is a framework through which measurement information is synthesized with *a priori* information, producing an estimate of a species distribution. In Bayesian CST, the measurement data and inferred parameters are conceptualized as random variables, characterized by a probability density function (pdf). Measurements are then used to update the distribution parameters and estimate $\mathbf{x}$. Bayesian CST begins with Bayes' relation

$$\pi\left(\mathbf{x} \mid \mathbf{b}\right) = \frac{\pi\left(\mathbf{b} \mid \mathbf{x}\right) \pi_{\text{pr}}\left(\mathbf{x}\right)}{\pi\left(\mathbf{b}\right)} \propto \pi\left(\mathbf{b} \mid \mathbf{x}\right) \pi_{\text{pr}}\left(\mathbf{x}\right), \tag{4}$$

where $\pi(\mathbf{x}|\mathbf{b})$ gives the probability density for $\mathbf{x}$ after the measurement $\mathbf{b}$; $\pi(\mathbf{b}|\mathbf{x})$ is the likelihood, which assigns the probability of observing $\mathbf{b}$ for a hypothetical distribution $\mathbf{x}$; $\pi_{\text{pr}}(\mathbf{x})$ is the prior, which encodes information known about the flow before a measurement $\mathbf{b}$; and $\pi(\mathbf{b})$ is the evidence, which scales the numerator to conserve total probability. In most applications the

reconstruction is visualized in terms of the maximum *a posteriori* (MAP) estimate $\mathbf{x}^{\text{MAP}} = \text{argmax}\{\pi(\mathbf{x}|\mathbf{b})\}$, along with some measure of uncertainty. Calculating $\mathbf{x}^{\text{MAP}}$ requires a likelihood function and prior distribution.

Instantaneous measurements from the photovoltaic detector are corrupted by a combination of photonic shot noise, which obeys a Poisson distribution, and normally-distributed electronic noise [42]. Shot noise can be modeled as Gaussian given the large number of photons collected per measurement [43]. In the case of time-averaged measurements of a turbulent flow, the contribution of measurement noise is small compared to fluctuations caused by random variation in the flow field. In all cases, the measurement noise can be modeled as independent and identically distributed (IID) with standard deviation σ_m [44], which can be characterized through a statistical analysis of the data [30].

For normally-distributed IID noise, the probability of observing the data $\mathbf{b}$ for a hypothetical distribution $\mathbf{x}$ is given by

$$\pi(\mathbf{b}\,|\,\mathbf{x}) = \frac{1}{\left(2\pi\sigma_m^2\right)^{n/2}} \exp\left\{-\frac{1}{2\sigma_m^2}\left(\mathbf{Ax}-\mathbf{b}\right)^T\left(\mathbf{Ax}-\mathbf{b}\right)\right\}. \tag{5}$$

Since $\mathbf{A}$ is rank-deficient, an infinite set of $\mathbf{x}$ vectors will maximize Eq. (5) for any $\mathbf{b}$, and many of these are physically-implausible [30]. Information about the plausibility of different candidate distributions must therefore be introduced through a structured prior. This added information is encoded in a pdf that assigns a probability density to $\mathbf{x}$ in line with *a priori* knowledge about the target species distribution. Turbulent fluid flows are frequently cast as random variables [45] and concentration data can be modelled as a joint-normal random variable $\mathbf{x} \sim \mathcal{N}(\boldsymbol{\mu}, \boldsymbol{\Gamma}_\mathbf{x})$ [46], where $\boldsymbol{\mu}$ is the mean distribution and $\boldsymbol{\Gamma}_\mathbf{x}$ is the spatial covariance of the flow. The resulting prior pdf is

$$\pi_{\text{pr}}(\mathbf{x}) = \frac{1}{\sqrt{(2\pi)^n |\boldsymbol{\Gamma}_\mathbf{x}|}} \exp\left\{-\frac{1}{2}(\mathbf{x}-\boldsymbol{\mu})^T \boldsymbol{\Gamma}_\mathbf{x}^{-1}(\mathbf{x}-\boldsymbol{\mu})\right\}. \tag{6}$$

Since the arguments of Eqs. (5) and (6) are in the exponential function, the posterior pdf is itself proportional to an exponential [30]

$$\pi(\mathbf{x} \mid \mathbf{b}) \propto \exp\left\{ -\frac{1}{2} \left\| \begin{bmatrix} \sigma_m \mathbf{A} \\ \mathbf{L} \end{bmatrix} \mathbf{x} - \begin{bmatrix} \sigma_m \mathbf{b} \\ \mathbf{L}\boldsymbol{\mu} \end{bmatrix} \right\|_2^2 \right\},$$ (7)

where $\mathbf{L} = \mathrm{chol}(\boldsymbol{\Gamma}_\mathbf{x}^{-1})$ is the Cholesky factor of the inverse covariance matrix. The MAP estimate is found by minimizing the norm in Eq. (7)

$$\mathbf{x}^{\mathrm{MAP}} = \min_{\mathbf{x}} \left\{ \left\| \begin{bmatrix} \sigma_m \mathbf{A} \\ \mathbf{L} \end{bmatrix} \mathbf{x} - \begin{bmatrix} \sigma_m \mathbf{b} \\ \mathbf{L}\boldsymbol{\mu} \end{bmatrix} \right\|_2^2 \right\}.$$ (8)

Following the specification of $\boldsymbol{\mu}$ and $\boldsymbol{\Gamma}_\mathbf{x}$, tomographic reconstruction amounts to solving Eq. (8).

Reconstruction accuracy depends strongly on the choice of $\boldsymbol{\mu}$ and $\boldsymbol{\Gamma}_\mathbf{x}$, which, in turn, depends on the type of prior information known about the flow field. Daun *et al.* [30] and Grauer *et al.* [46] present several candidate prior distributions for turbulent flow. When little is known about the flow structure, it may suffice to assume that the flow will be spatially-smooth, based on a diffusion-dominated transport model. This assumption is realized by way of first-order Tikhonov regularization [48], where $\boldsymbol{\mu} = 0$ and the $\mathbf{L}$ matrix is constructed as

$$l_{ij} = \begin{cases} 1, & i = j \\ -n_i^{-1}, & d_{ij} = 1 \\ 0, & \text{otherwise} \end{cases},$$ (9)

where n_i is the number of pixels bordering the ith pixel and d_{ij} is the pixel-wise distance between i and j. $\mathbf{L}$ is multiplied by the regularization parameter λ, which, in the Bayesian framework, implies a "Tikhonov covariance" $\boldsymbol{\Gamma}_{\mathrm{Tik}} = (\lambda^2 \mathbf{L}_{\mathrm{Tik}}^T \mathbf{L}_{\mathrm{Tik}})^{-1}$. We selected $\lambda = 0.20$ using the procedure developed by Daun [48].

Reconstruction can be further improved by taking the product of the prior in Eq. (6) and a concentration range prior

$$\pi_{cr}(\mathbf{x}) = \begin{cases} 1, x_{i \in 1,\dots,n} \in [x_{\min}, x_{\max}] \\ 0, \qquad \text{otherwise} \end{cases},$$ (10)

where $[x_{\min}, x_{\max}]$ is a physically-motivated constraint on x_j coefficients. (This range is $[0, \infty)$ for κ_η.) $\mathbf{x}^{\mathrm{MAP}}$ is then found by solving Eq. (8) subject to bound constraints in Eq. (10) using a constrained least squares algorithm.

2.2 Broadband CST

2.2.1 Measurement principle

The reconstruction procedure described above transforms a set of monochromatic light intensity measurements over a single absorption line into a spatially-resolved estimate of the absorption coefficient κ_η. Broadband detectors yield a voltage due to light incident over a measurement band $\eta_{1-2} \in [\eta_1, \eta_2]$ that includes significant absorption by the target species (*i.e.*, many strong lines) and negligible absorption by other gasses in the measurement field. Since κ_η is highly non-uniform over the measurement band, due to the complex line structure of gas molecules, broadband light absorption cannot be approximated by simple modifications of Eq. (1), for instance by substituting mean values of $I_{0\eta}$ and κ_η over η_{1-2} into Eq. (1). Instead, we must derive a suitable broadband operator that relates broadband transmittance to the path-integrated gas concentration.

At atmospheric pressures, ro-vibrational lines have a Lorentzian profile f_L due to collision broadening [49]

$$f_L(\eta;\eta_{ij}) = \frac{\gamma_c / \pi}{\gamma_c^2 + (\eta - \eta_{ij})^2}, \tag{11}$$

where η_{ij} is the centre wavenumber of the transition *ij* and γ_c is the collision half-width at half maximum (HWHM). The HWHM is specific to a mixture and depends on the local temperature T, pressure p, and volume fraction χ of the gas. For a gas mixture, γ_c is the partial pressure-weighted sum of molecule-specific FWHMs

$$\gamma_{c,i}(p_i, \chi_i) = \left[p_i \gamma_{self,i} + (1 - p_i)\gamma_{air,i} \right], \tag{12}$$

where $p_i = \chi_i \cdot p$ is the partial pressure of the ith gas, and $\gamma_{self,i}$ and $\gamma_{air,i}$ are the self- and air-broadened HWHMs of *i*, respectively. Finally, the mass spectral absorption coefficient for a mixture is the sum of transition-specific lines scaled by a number density

$$\kappa_\eta = \sum_{ij} S_{ij} f_L(\eta;\eta_{ij}, T, p, \chi) \cdot \frac{p\chi}{k_B T}, \tag{13}$$

where k_B is the Boltzmann constant. This treatment applies to mixtures near ambient conditions, where collision broadening dominates other forms of local line broadening, and where interspecies

line broadening is minimal. Figure 2 illustrates the collision-broadened absorption spectral of CH_4, C_2H_4, and C_3H_8 in the mid-IR spectrum.
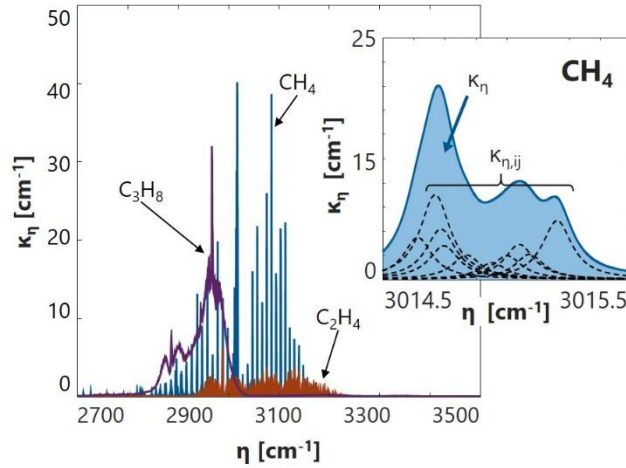

Figure 2: Absorption coefficient profiles of CH₄, C₂H₄, and C₃H₈ in the mid-IR region: the total absorption coefficient is a summation of Lorentz-shaped lines, seen for CH₄ in the inset.

Line strength, collision half-width, and transition wavenumber data for simple hydrocarbons are included in spectral line databases such as HITRAN [40]. The spectral absorption coefficient of more complex molecules can be inferred from empirically-derived transmittance profiles, *e.g.* [41]. This data may then be used to compute a broadband transmittance. For a thermal emitter-light detector pair, separated by a distance L, the power P incident on the detector is calculated as

$$P = \int_{\eta_{1-2}} C_g f_\eta \epsilon_\eta I_{b\eta}(T) \exp\left\{-\int_0^L \kappa_\eta(u)\,du\right\} d\eta, \qquad (14)$$

where η_{1-2} is the spectral range of the filter applied to the detector; C_g is a configuration factor, which accounts for the fraction of rays that reach the detector due to geometric considerations; f_η is the detector's photovoltaic diode efficiency; ϵ_η is the emissivity of the source; $I_{b\eta}$ is the intensity of a blackbody emitter at the source temperature T; and κ_η is the absorption coefficient of the target species at u. The absorption coefficient is the only parameter in Eq. (14) that varies significantly with respect to wavelength across the filter window. As such, the remaining parameters of Eq. (14) can be grouped together into an emitter-detector constant C_{e-d}.

A broadband transmittance T is defined as the ratio of the power during an absorption measurement P_{abs} to the reference power P_{ref}, which corresponds to a measurement without the target species (*i.e.* $\kappa_\eta = 0$)

$$P_{ref} = C_{e-d} \int\limits_{\eta_{1-2}} \exp\left\{-\int_0^L (0)\,du\right\} d\eta = C_{e-d}\Delta\eta_{1-2}, \tag{15}$$

where $\Delta\eta_{1-2} = \eta_2 - \eta_1$. C_{e-d} cancels out in the transmittance expression, which leaves

$$T = \frac{P_{abs}}{P_{ref}} = \frac{1}{\Delta\eta_{1-2}} \int\limits_{\eta_{1-2}} \exp\left\{-\int_0^L \kappa_\eta(u)\,du\right\} d\eta. \tag{16}$$

In contrast to monochromatic OP measurements, the broadband transmittance in Eq. (16) is a nonlinear function of the target's path-integrated concentration. Consequently, an additional step is required to deconvolve the species concentration distribution from broadband measurements.

2.2.2 Linear broadband measurements

Photonic absorption events are independent. Moreover, the mass line strength is a linear function of the partial pressure of the target species, as seen in Eq. (13). A corollary of these observations is that the absorption coefficient can be represented as a product of the local concentration and a spectral shape function C_η. When temperature and pressure conditions are constant, so long as the self- and air-broadened collision half-widths are comparable, C_η will be effectively independent of the concentration. Therefore, we can represent κ_η as

$$\kappa_\eta = \chi(u)\cdot C_\eta, \tag{17}$$

where $\chi(u)$ is the volume fraction of the target species at u; and C_η is the sum $\Sigma_{ij}(S_{ij}\cdot f_L)$ scaled by $p/(k_B\cdot T)$.

The decomposition in Eq. (17) breaks down when the self- and air-broadened HWHMs of a molecule differ significantly, but these differences are naturally mitigated and the decomposition is only problematic in special cases. That is, total absorption approaches zero as the number of target molecules approaches zero, and the role of air-broadening is proportional to the fraction of air in the mixture. As a result, the absolute error due to divergent HWHMs is inherently diminished.

10

Substituting Eq. (17) into Eq. (16) results in the following expression for transmittance

$$T = \frac{1}{\Delta\eta_{1-2}} \int_{\eta_{1-2}} \left[\exp\left\{ -\int_0^L \chi(u)\,du \right\} \right]^{C_\eta} d\eta \,. \tag{18}$$

Next, we define G as the path-integrated concentration of the target species from 0 to the detector at L

$$G(L) \equiv \int_0^L \chi(u)\,du \,. \tag{19}$$

Substituting G into Eq. (18) yields

$$T = \frac{1}{\Delta\eta_{1-2}} \int_{\eta_{1-2}} \left[\exp\left\{ -G(L) \right\} \right]^{C_\eta} d\eta \,, \tag{20}$$

which can be computed for a species with known C_η over a set detection range. Once this computation has been carried out, the inverse of G can be constructed numerically such that

$$b_i \equiv G(L) = G^{-1}(T, C_\eta) \,, \tag{21}$$

where b_i is the path-integrated volume fraction of the target and $G^{-1}(T, C_\eta)$ is a linearizing "transfer function."

Due to the shared form of Eqs. (2) and (19), the ray-sum **A**, described in Section 2.1, relates the target distribution **x** to a data vector **b** that contains path-integrated volume fraction data, found using Eq. (21). Moreover, given p and T, the volume fraction relates to a mass fraction. As such, the Bayesian reconstruction procedure from Section 2.1 may be applied directly to reconstruct the target distribution. The linearization of broadband measurements is valid under the following conditions:

1. Absorption is the prevailing mode of radiative transfer;
2. Collision broadening dominates the line shape;
3. Self- and air-broadened collision half-widths are comparable; and
4. The chemical composition of the target species is homogenous.

3 Experimental Apparatus and Procedure

3.1 Measurement device

A custom-built OP measurement device was developed to make the multiple absorption measurements needed to carry out broadband CST. The prototype system consisted of four transmitter-receiver pairs. The transmitter and receiver units were assembled from low-cost, commercially-available components to facilitate development of a large number of units, capable of making time-resolved measurements in future experiments. Following this philosophy, the objective of this tomography system is to determine the spatial distribution of a single species concentration (or that of a homogeneous mixture concentration), and not to distinguish the components of a mixture.

Each transmitter consisted of a 5 mm long, 1 mm diameter silicon nitride glowbar (HawkEye Technologies IR-Si243), positioned within a parabolic reflector (Phoenix PA10.02) having an opening diameter of 97.8 mm, shown in Figure 3.
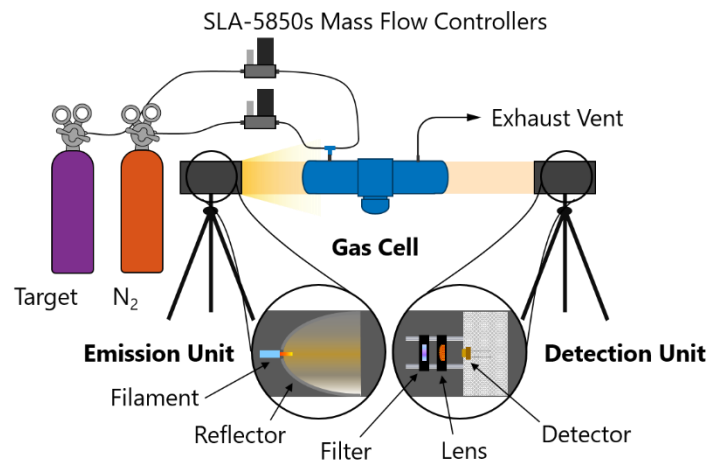

Figure 3: Emitter and detector for OP broadband measurement and a calibration schematic, featuring an absorption cell that contains a controlled mixture of N_2 and the target species.

The assembly was housed within a cylindrical aluminum case and mounted on an adjustable tripod base. The filament was powered using a 12 V, 1.6 A supply, which produced a filament temperature of 1443 K. The optimal filament position within the reflector was determined using a Monte Carlo ray-tracing procedure, set to maximize the fraction of collimated light.

The receiver consisted of a 25.4 mm (1") diameter CaF plano-convex lens (ThorLabs LA5470-E) that focused incident light onto an uncooled InAs photovoltaic (PV) detector (Hamamatsu P10090-01), equipped with a bandpass filter (ThorLabs FB3250-500 IR). The PV detector has a nearly-uniform response over filter's spectral window. Optical components were cage-mounted within an aluminum cylinder, which in turn was mounted on an adjustable tripod. Detector voltages were amplified (TI LM358) and collected with a USB-6001 DAQ from National Instruments. Running the emitter-detector pair without the target gas, we observed normally-distributed noise with a standard deviation equal to 0.3% of the signal.

The transmitter and receiver were aligned with a removable assembly consisting of a visible diode laser, mounted over the transmitter, and a mirror, mounted over the receiver. The alignment assembly was removed prior to measurement.

3.2 Calibration procedure

Transfer functions, derived in Section 2.2, were validated by examining the response of the transmitter/receiver system to known dilutions of CH_4, C_2H_4 and C_3H_8 in nitrogen (N_2). These measurements were made using a gas cell, depicted in Figure 3, having a total path length of 81 cm between two 38.1 mm (1.5") diameter sapphire windows. For each measurement, a flow of N_2 and a flow of the target gas were supplied through two ports, and controlled using either a mass flow controller (CH_4: Brooks SLA-5850S) or rotameters (C_2H4, C_3H_8: Cole Parmer N102-05; N_2: Cole Parmer N034-39). The volume fraction of the target species was adjusted from 0 (*i.e.* P_{ref}) to 1, with between 16 and 22 measurements in between. Measurements were recorded after P_{abs} remained constant for five minutes, thus ensuring the gas mixture in the cell had stabilized. Absorption measurements were supplemented with point-concentration measurements, made with an FID (ThermoScientific TVA-1000A).

4 Results and Discussion

4.1 Developing measurement transfer functions

Line strength and collision half-width parameters are available for both CH_4 and C_2H_4 in the HITRAN database [40]. Line shapes were calculated using Eq. (11), summed per Eq. (12), and scaled by ρ/m_g, resulting in κ_η in units of cm^{-1}. Division by $c = 10^6$ ppm gave C_η. Transmittances were calculated for a 5,000-point discretization of the mid-IR spectrum from 2,000 to 4,000 cm^{-1}. Absorbance data for C_3H_8 were inferred from the high resolution FTIR absorbance measurements reported in [41]. Measurements in [41] were made using a 1 ppm·m burden of C_3H_8 at 296 K and pressures ranging from 0.45 to 12.10 Torr. We scaled the absorbance data by $\ln(10)\cdot 10^6$ cm^{-1} to obtain κ_η, assuming a linear function of partial pressure and a negligible difference between self- and air-broadened collision half-widths.

Figure 4 shows manufacturer-supplied bandpass filter transmittance data imposed on absorption spectra for CH_4 at 1 atm.
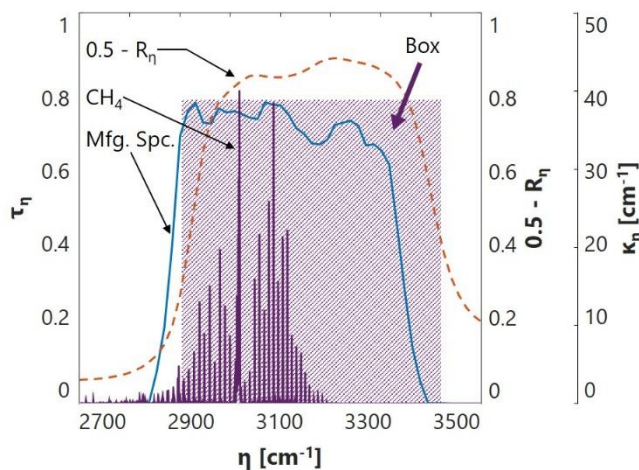

Figure 4: Manufacturer-supplied filter transmittance data; absorption spectra for CH4 at 1 atm; FTIR-measured filter reflectance data; and the transmittance results of a box regression analysis.

The filter width is known to a tolerance of ±0.10 μm and the centre wavelength to ±0.05 μm. Due to the large number of spectral lines close to the lower filter window threshold (~2,850 cm^{-1}), transmittance measurements are sensitive to the precise onset and slope of the window. Transmittance measurements are independent of the peak filter transmissivity, however, as the

transmission range is approximately constant. τ_η is therefore grouped into the constant C_{e-d}, which cancels out in Eq. (16). This procedure amounts to a box model of the bandpass filter, *i.e.* with a uniform spectral transmittance over the filter window, and opaque outside the window.

Filter bounds for the box model were inferred by carrying out a nonlinear regression between modeled and measured transmittances for dilutions of CH_4 in N_2, C_2H_4 in N_2, and C_3H_8 in N_2, ranging from 0% to 100%. The regression gave a filter centred on $\eta_c = 3163$ cm^{-1} of width $\eta_w = 523$ cm^{-1}. This range was consistent with the filter's reflectance profile, measured with a FTIR reflectometer (Surface Optics Corp. SOC-400), also shown in Figure 4. The corresponding measured and modeled transmittances are plotted in Figure 5.
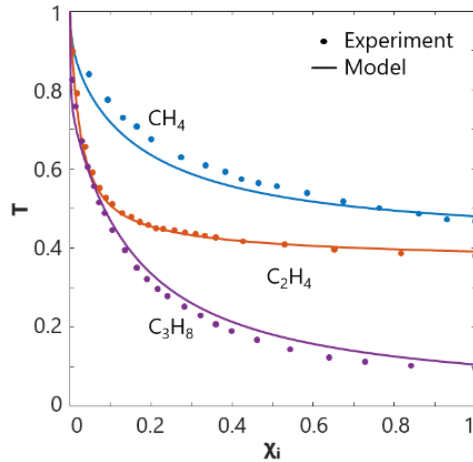

Figure 5: Modelled and measured transmittances for CH₄, C₂H₄, and C₃H₈.

The box filter bounds were used to compute a database of T for the target species, *via* Eq. (20), over path-integrated concentrations ranging from 1 to 10^6 ppm·m. This database was then used to construct the transfer functions $G^{-1}(T, C_\eta)$, plotted in Figure 6. The transfer function is a monotonic map of broadband measurements of T to linear, path-integrated concertation data, suitable for tomographic reconstruction.
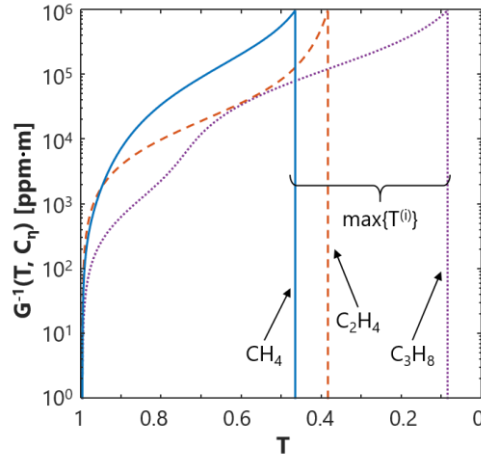
Figure 6: Broadband CST transfer functions for CH$_4$, C$_2$H$_4$, and C$_3$H$_8$ for a box filter with η_c = 3163 cm^{-1} and η_w = 523 cm^{-1}.

4.2 Lab-scale tomography experiment

The broadband tomography methodology was evaluated by reconstructing a C$_3$H$_8$ plume generated within an enclosed test space, representative of a ground source fugitive emission (*e.g.*, [51,52]), except at a smaller scale. A 1×1 m domain was defined for the tomography experiment, shown in Figure 7a, with its origin in the centre. Propane was supplied at 2.44 L/min and released vertically into the domain through a 7.62 cm (3") diffuser located at $x = 0.21$ m, $y = 0.21$ m, and $z = 0.55$ m. A small fan, placed level with the plume, provided a 2 m/s flow of air from the corner of the domain. The domain size was chosen to be proportional to the size of the C$_3$H$_8$ source. Individual single-path measurements were conducted over a 10 m distance to verify that the transmitted light was collimated, and hence that the OP system could operate over distances relevant to field measurements.
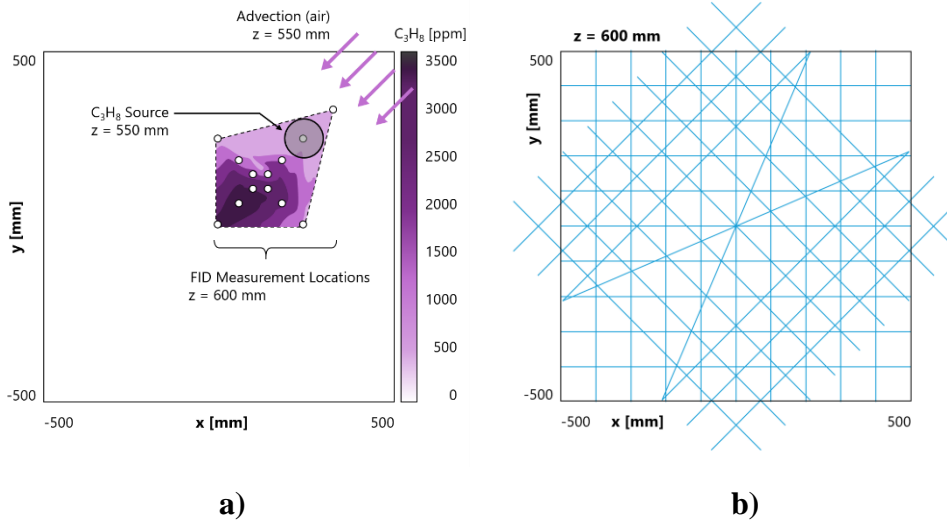
16

<center>a)   b)</center>

Figure 7: Setup and results of a C_3H_8 emissions detection experiment: a) C_3H_8 source, FID measurement positions, and C_3H_8 contour plot and b) line-of-sight measurement array.

An FID was used to calculate an average propane concentration at 13 discrete locations in the domain. Twelve FID measurements were made at each location over 5 second intervals. The average standard deviation of the measurements was 480 ppm, with a maximum standard deviation of 1603 ppm. Figure 7a shows the contours of a spline interpolation of the average FID measurements.

Transmittance measurements were carried out for a 35-beam, four-projection orthogonal measurement array, depicted in Figure 7b. Each projection of the 36-beam base arrangement contained nine beams, centred in the domain and spaced 10 cm apart. A single beam was excluded from one of the projections to accommodate the fan, and the two adjacent beams were crossed to partially compensate for the loss of information. Transmittance measurements began with a 600 s reference measurement, recorded at 2 Hz, after which C_3H_8 was introduced into the domain, commencing a 600 s absorption measurement, also recorded at 2 Hz. The ratio of the mean absorption to mean reference measurement was transformed by the $G^{-1}(T, C_\eta)$ function for C_3H_8 in Figure 6, giving a path-integrated concentration.

Our solution domain comprised a 20×20 square pixel basis and we closed the Bayesian CST framework with a Tikhonov prior. Figure 8 shows a contour plot of the reconstructed C_3H_8 plume. This reconstruction is consistent with the FID concentration measurements plotted in Figure 7a. Table 1 lists mean concentration data and uncertainties for the five largest FID

<center>17</center>

measurements and the corresponding values from the broadband CST reconstruction. (Uncertainty quantification for the CST data is reviewed in Section 4.3.) Table 1 demonstrates that C_3H_8 concentrations measured with the FID were broadly consistent with those found through CST. Integral scale fluctuations in the concentration of C_3H_8 resulted in large uncertainties in the FID measurements, which took place over a 60 s interval. The uncertainties of the CST measurements are smaller due to the longer time interval (300 s), and because CST measurements inherently average concentration data over space.
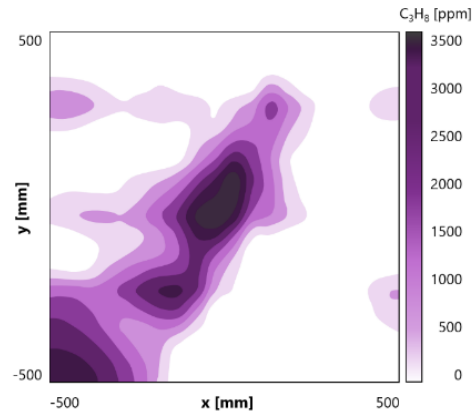

Figure 8: Broadband CST reconstruction of a C_3H_8 plume with advection.

Table 1: Comparison of concentration data in Figures 7a and 8 from FID measurements and broadband CST imaging, respectively.

Location		FID-based χ [ppm]		CST-based χ [ppm]	
x [mm]	y [mm]	μ	σ	μ	σ
-0.10	0.10	2894	725	3514	275
0.00	0.00	2595	860	3079	230
-0.15	0.15	1952	931	2594	285
0.20	0.15	1848	1603	2833	271
0.25	0.10	1691	863	1916	288

4.3   Error analysis

Error in broadband CST experiments can be divided into four categories: random measurement error; model error in the transfer function; regularization error, due to the incompatibility of the prior and the true solution; and discretization error.

Transmittance measurements are derived from the ratio of two random variables, the mean absorption and reference measurements, designated V_{abs} and V_{ref}, respectively. Figure 9 shows a typical set of measurement data used to obtain a transmittance.
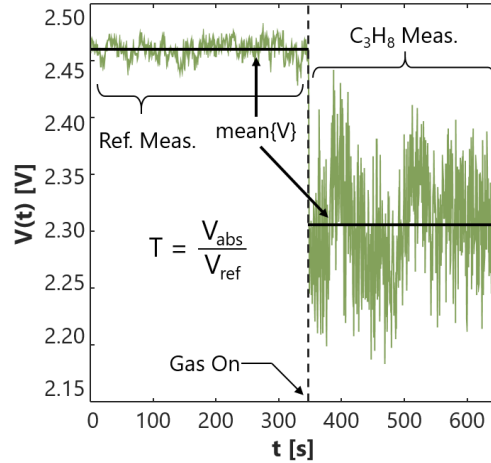

Figure 9: Voltages used to obtain a transmittance measurement.

The distribution of fluctuations in the reference measurement, indicative of electronic noise, roughly follows a normal distribution. The increased variation in the absorption measurement in Figure 9 is attributed to turbulent fluctuations in the C_3H_8 plume. These large-scale fluctuations indicate transient behaviour on time-scales longer than the FID measurement intervals, which could be imaged by a time-resolved broadband CST system.

According to the central limit theorem, the mean values V_{abs} and V_{ref} are normally distributed. For the measurement in Figure 12, these variables have standard deviations $\sigma_{abs} = 1.9 \cdot 10^{-3}$ V and $\sigma_{ref} = 2.8 \cdot 10^{-4}$ V, respectively. Expanding the variance of V_{abs}/V_{ref} and neglecting higher order terms, the variance of T is approximated as

$$\sigma_T^2 = \frac{V_{abs}^2 \sigma_{ref}^2 + V_{ref}^2 \sigma_{abs}^2}{V_{ref}^4}. \tag{22}$$

Equation (22) leads to the estimate $\sigma_T = 3.1 \cdot 10^{-5}$ for $T = 0.937$, calculated for the signal in Figure 12. We observed a maximum standard deviation of $\sigma_T = 1.6 \cdot 10^{-4}$ for a transmittance $T = 0.974$. Mean transmittances, therefore, were known to a high degree of precision.

Another source of error is the transfer function. Discrepancies between modelled and experimental transmittance data arose due to the simplifying assumptions required to obtain Eq. (16), *e.g.* modeling the bandpass filter response as a box filter. We approximated the C_3H_8 transfer function error by taking the normalized Euclidean distance between the transmittances from our calibration experiment and the transmittances predicted by our transfer function. This procedure showed a maximum discrepancy of 370 ppm·m for C_3H_8 burdens up to 6500 ppm·m (or 5.69%). Greater uncertainty is expected for higher burdens as partially-transmitted spectral lines at the filter wings, which are excluded by the box filter model, absorb more light.

Finally, the tomographic reconstruction process is subject to errors associated with the discretization scheme and error due to the incompatibility between the prior and true distribution. We used a Bayesian CST framework with non-negative square pixels and a Tikhonov covariance. Qualitatively, this procedure yields estimates that have been shown to resemble the ground truth distribution [30,46,48].

Figure 10 illustrates the sensitivity of reconstructions to the density and arrangement of measurement lines. Using different subsets of the measurement data, reconstructions roughly capture the measurement plume peak, but differ at the margins. This limitation may be overcome with supplementary measurement lines or by developing a more sophisticated prior.
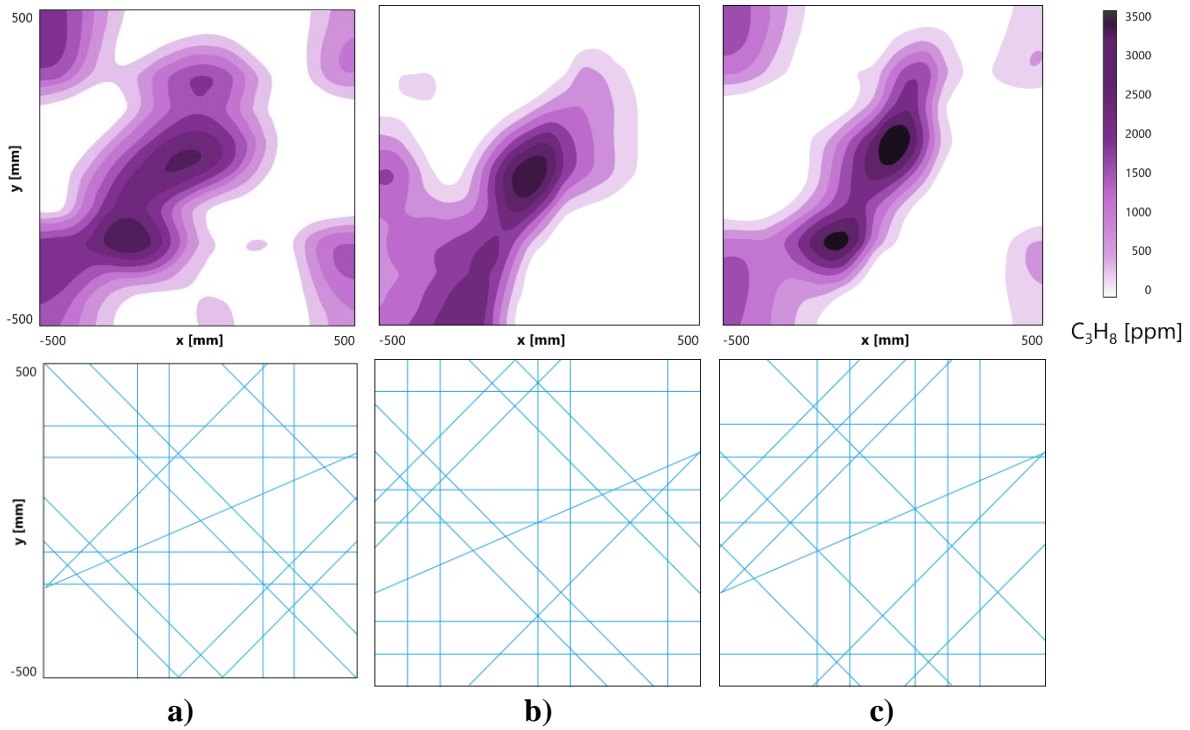
Figure 10: Alternative reconstructions using a subset of the measurement data and the corresponding measurement lines: a) half of each projection; b) compliment arrangement to (a); and c) 18 randomly-selected measurement lines.
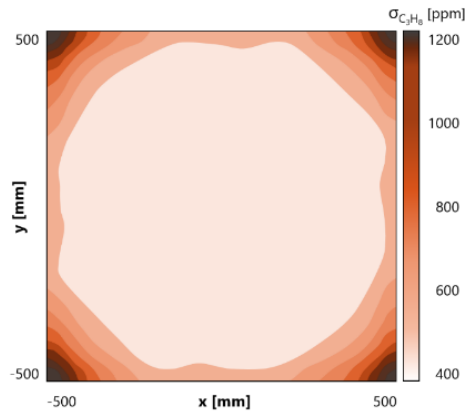

Figure 11: Map of the estimated posterior standard deviation of the mean C_3H_8 distribution.

A quantitative estimate of reconstruction uncertainty was obtained by analyzing the difference between ground truth plumes and tomographic reconstructions from Grauer *et al.* [54], ensuring basis and regularization parameter parity. The mean net and maximum concentration errors were found to be 31% and 14%, respectively. An estimate of the posterior covariance matrix

21

was then calculated using Eq. (18) of Grauer *et al.* [54]. This equation gives $\mathbf{\Gamma_x}$ for $\pi(\mathbf{x|b})$, which reveals how the operator $\mathbf{A}$ propagates uncertainty in the prior. Figure 14 shows a contour map of the resulting posterior standard deviation for our C_3H_8 reconstruction. Regions of high uncertainty in Figure 14 align with artefacts in the plume reconstruction in Figure 11, primarily concentrated about the corner $x = $ -0.5 m, y = -0.5 m.

4.4   Discussion

Broadband CST is a three-stage process. First, transmittance measurements are taken. Next, these measurements are transformed into a path-integrated concentration. Finally, transformed measurements are tomographically reconstructed. A proof-of-concept laboratory-scale experiment showed that the reconstruction of a C_3H_8 plume, given in Figure 11, was consistent with point concentrations measured with an FID, given in Figure 10a. An error analysis of those results suggested similar levels of point-wise uncertainty in the FID and CST estimates. Uncertainty in the FID measurements arose due to the transient nature of the plume, while uncertainty in the tomographic estimate arose due to modelling errors in the transfer function and regularization error from the reconstruction procedure. Here we discuss each stage of broadband CST and comment on the viability of broadband CST as an emissions diagnostic.

Transmittance measurements are straightforward for stationary or time-averaged flows. Both the reference and absorption signals are average quantities, robust to the measurement duration at the margin of the interval, and uncertainty about the transmittance is limited. Moreover, the simplicity and low-cost of the detection apparatus lends itself to the simultaneous measurements needed to capture integral-scale turbulent fluctuations, which are needed to calculate an emissions flux. A real-time reference measurement could be established using a filter wheel with filters both transparent and opaque to the target's absorption bands, serving as absorption and reference measurements, respectively. Moreover, with the accumulation of measurement data over time, previous measurements could be used to improve the prior by way of covariance estimation [46].

The theoretical transmittances plotted in Figure 8 underline the importance of filter selection. While the $C_{e\text{-}d}$ introduces a modelling error due to spectral variation in f_η, ϵ_η, and $I_{0\eta}$ over $\eta_{1\text{-}2}$, the primary source of error is the box filter assumption. The onset of transmission, around 2900 cm^{-1}, is not known with precision, as evidenced by the discrepancy between the

manufacturer-provided transmission data and the reflectance measurement in Figure 7. The target gasses featured different levels of absorption in this region. The spectral lines of C_3H_8 are dense and overlap substantially near the filter's edge; CH_4 also absorbs light around this onset, but less so than C_3H_8; conversely, the bulk of C_2H_4 absorption lies well within the filter window. The amount of absorption at the filter boundary corresponds to modelling error: 6.2%, 4.7%, and 3.4% for C_3H_8, CH_4, and C_2H_4, respectively. In order to minimize this error, filter selection should seek to minimize overlap of the transmission range and target absorption bands.

Uncertainty in the recovered concentration distribution was dominated by uncertainty due to the tomography procedure. Since the measurement model developed in this paper yields an IFK, identical in form to the classical CST measurement model, general algorithmic improvements to limited-data CST can be applied directly to broadband CST. One avenue for improvement lies in the development of the prior. Estimating the mean and covariance of turbulent variables using simulated or published data has been shown to notably improve reconstructions, compared to the relatively uninformative smoothness prior used in this work [46]. Moreover, optimization of the measurement array based on prior knowledge of the concentration distribution can improve reconstructions, as well [54].

Our results demonstrate the potential for a passive, OP, spatially-resolved, quantitative emissions diagnostic. The uncertainty of FID measurements for a time-varying flow, due to turbulent fluctuations in the gas, was comparable to the uncertainty of the CST results. Collecting FID measurements was labour-intensive and required direct physical access to the measurement points. In contrast, broadband OP measurements can be operated remotely and only require optical access. Tomographic reconstruction yields spatially-resolved data through deconvolution, rather than through extrapolation or dense arrays of labour-intensive probe measurements. As such, broadband tomography is a promising avenue for emissions detection research.

5   Conclusion

The need to develop stand-off measurement techniques for detecting and quantifying hydrocarbon emissions is motivated by their contributions to climate change, and the numerous health and safety hazards they present to workers and the public at large. This paper develops the measurement theory for broadband chemical species tomography, a novel approach to the spatially-resolved quantification of emissions, and the results of a proof-of-concept emission detection experiment.

Previous CST deployments have been based on spectrally-resolved light intensity data, in which case the monochromatic transmittances that form the basis for reconstruction are related to the spectral absorption coefficient through a linear (Fredholm) integral equation of the first kind. In contrast, broadband measurements convolve this IFK over the detector's spectral range. The measurement model we use for tomographic reconstruction begins with a transfer equation that maps broadband transmittances to a path-integrated concentration. These functions derive from individual line or spectral absorbance data in the literature. Path-integrated concentrations are finally deconvolved using a Bayesian procedure that explicates the essential role of prior information.

Using this system, we conducted a broadband CST experiment on a C_3H_8 plume with advection and validated our results using FID measurements. The tomographically-reconstructed C_3H_8 concentrations were consistent with our FID measurements. This experiment constitutes the first spatially-resolved, open-path broadband emission tomography experiment and suggests a rich avenue for further research.

One such avenue concerns mass flux estimation. While it is desirable to estimate the mass rate of an emissions molecule, the present technique yields a 2D concentration map. Broadband CST can be extended to three dimensions, which enables simple estimation of the mass rate. However, it is also possible, in principle, to combine maps of concentration and variance data with a plug flow model of the gas to generate an estimate of the mass flux. Another concern is the presence of a highly-absorbing non-target species, such as water vapour, which can affect the transfer function. It is possible to augment the transfer function, adjusting it to account for an average concentration of water vapour. However this procedure would introduce error into the path-integrated concentration estimate.

Future work will focus on the development of prior pdfs, the construction of a real-time broadband CST device, and the quantification of error due to presence of non-target species.

References

[1]   J. Dewulf and H.V. Langenhove, "Anthropogenic volatile organic compounds in ambient air and natural waters: a review on recent developments of analytical methodology, performance and interpretation of field measurements," *J. Chromatogr. A*, **843**, pp. 163–177, 1999.

[2]   D. Krewski, R. Snyder, P. Beatty, G. Granville, B. Meek and B. Sonawane, "Assessing the health risks of benzene: a report on the benzene state-of-the-science workshop." *J. Toxicol. Env. Health A*, **61**.5-6, pp. 307-338, 2000.

[3]   Y. Dumanoglu, M. Kara, H. Altiok, M. Odabasi, T. Elbir and A. Bayram, "Spatial and seasonal variation and source apportionment of volatile organic compounds (VOCs) in a heavily industrialized region," *Atmos. Env.*, **98**, pp. 168-178, 2014.

[4]   R. K. Pachauri and L. Meyer, "Climate change 2014: synthesis report. Contribution of working groups I, II and III to the fifth assessment report of the intergovernmental panel on climate change," *IPCC*, Geneva, Switzerland, 2014.

[5]   EPA, Method 25A - Determination of total gaseous organic concentration using a flame ionization analyzer. *EPA*, Washington, DC, 2007.

[6]   E. Jones, "The pellistor catalytic gas detector," in *Solid-State Gas Sensors*, 1st ed. Boca Raton, FL: CRC Press, Ch. 2, pp. 17–31, 1987.

[7]   EPA, Method 21 - determination of volatile organic compound leaks. *EPA*, Washington, DC, 2007.

[8]   E. Bakker and M. Telting-Diaz, "Electrochemical sensors," *Anal. Chem.*, **74**.12, pp. 2781-2800, 2002.

[9]   M.N. Fiddler, I. Begashaw, M.A. Mickens, M.S. Collingwood, Z. Assefa and S. Bililign, "Laser spectroscopy for atmospheric and environmental sensing," *Sensors*, **9**.12, pp. 10447-10512, 1999.

[10]   S.B. Schoonbaert, D.R. Tyner and M.R. Johnson, "Remote ambient methane monitoring using fiber-optically coupled optical sensors," *Appl. Phys. B*, **119**.1, pp. 133-142, 2015.

[11]   J.G. Watson, J.C. Chow and E.M. Fujita, "Review of volatile organic compound source apportionment by chemical mass balance," *Atmos. Env.*, **35**.9, pp. 1567-1584, 2001.

[12]   A. Chambers, M. Strosher, T. Wootton, J. Moncrieff and P. McCreadyay, "DIAL measurements of fugitive emissions from natural gas plants and the comparison with emission factor estimates," in *Proceedings of the 15th International Emissions Inventory Conference*, New Orleans, LA, 2006.

[13]   A. Cuclis, "Why emission factors don't work at refineries and what to do about it," in *Proceedings of the 21st International Emissions Inventory Conference*, Tampa, FL, 2012.

[14]   G.G. Gimmestad, "Differential-absorption lidar for ozone and industrial emissions," in *Lidar Range-Resolved Optical Remote Sensing of the Atmosphere*, Singapore: Springer, Ch. 7, pp. 187-212, 2005.

[15]   L. Frisch. *Fugitive VOC-emissions measured at oil refineries in the province of Västra Götaland in South West Sweden*. County Admin. Board Västra Götaland, Göteborg, Sweden, Rep. 2003:56, 2003.

[16]   A.K. Chambers, M. Strosher, T. Wootton, J. Moncrieff and P. McCready, "Direct measurement of fugitive emissions of hydrocarbons from a refinery," *J. Air Waste Manage. Assoc.*, **58**.8, pp. 1047-1056, 2008.

[17]   R. Robinson, T. Gardiner, F. Innocenti, P. Woods and M. Coleman, "Infrared differential absorption Lidar (DIAL) measurements of hydrocarbon emissions," *J. Env. Monitor.*, **13**.8, pp. 2213-2220, 2008.

[18]   R. Hashmonay, "Optical remote sensing of fugitive VOC losses," in *2009 Spring Meeting & 5th Global Congress on Process Safety*, Tampa, FL, 2009.

[19]   R. Robinson, T. Gardiner, F. Innocenti, P. Woods and M. Coleman, "Infrared differential absorption lidar (DIAL) measurements of hydrocarbon emissions," *J. Env. Monitor.*, **13**.8, pp. 2213-2220, 2011.

[20]   D. Hoyt and L.H. Raun, "Measured and estimated benzene and volatile organic carbon (VOC) emissions at a major US refinery/chemical plant: comparison and prioritization," *J. Air Waste Manage. Assoc.*, **65**.8, pp. 1020-1031, 2015.

[21]   R.A. Hashmonay and S.H. Ramsey, "Long-term, open-path emissions monitoring at oil and gas exploration and production sites," in *Proceedings of the 21st International Emissions Inventory Conference*, Tampa, FL, 2012.

[22]   EPA, In oil and natural gas sector: new source performance standards and national emission standards for hazardous air pollutants reviews. *EPA*, Washington, DC, 2011.

[23]   M. Lackner, "Tunable diode laser absorption spectroscopy (TDLAS) in the process industries–a review," *Rev. Chem. Eng.*, **23**.2, pp. 65-147, 2007.

[24]   U. Platt and J. Stutz. *Differential absorption spectroscopy*. Berlin, Germany: Springer-Verlag, 2008.

[25]   A.M. Winer and H.W. Biermann, "Long pathlength differential optical absorption spectroscopy (DOAS) measurements of gaseous HONO, NO2 and HCNO in the California South Coast Air Basin," *Res. Chem. Intermed.*, **20**.3-5, pp. 423-445, 1994.

[26]   R.A. Hashmonay, R.M. Varma, M.T. Modrak, R.H. Kagann, R.R. Segall and P.D. Sullivan "Radial plume mapping: a US EPA test method for area and fugitive source emission monitoring using optical remote sensing," in *Advanced Environmental Monitoring*, 1st ed., Dordrecht, Netherlands: Springer, Ch 2, pp. 21-36, 2008.

[27]   A. Babilotte, T. Lagier, E. Fiani and V. Taramini, "Fugitive methane emissions from landfills: field comparison of five methods on a French landfill," *J. Environ. Eng.*, **136**.8, pp. 777-784, 2010.

[28]   B. Galle, J. Samuelsson, B.H. Svensson and G. Börjesson, "Measurements of methane emissions from landfills using a time correlation tracer method based on FTIR absorption spectroscopy," *Env. Sci. Technol.*, **35**.1, pp. 21-25, 2001.

[29]   C.F. Wu, T.G. Wu, R.A. Hashmonay, S.Y. Chang, Y.S. Wu, C.P. Chao, C.P. Hsu, M.J. Chase and R.H. Kagann, "Measurement of fugitive volatile organic compound emissions from a petrochemical tank farm using open-path Fourier transform infrared spectrometry," *Atmos. Env.*, **82**, pp. 335-342, 2015.

[30]   K.J. Daun, S.J. Grauer and P.J. Hadwin, "Chemical species tomography of turbulent flows: discrete ill-posed and rank deficient problems and the use of prior information," *J. Quant. Spectrosc. Radiat. Transfer*, **172**, pp.58-74, 2016.

[31]   H. McCann, P. Wright and K.J. Daun, "Chemical species tomography," in *Industrial Tomography Systems and Applications*, 1st ed. Cambridge, UK, Woodhead Publishing, 2015, Ch. 3, pp. 135–174, 2015.

[32]   W. Cai and C.F. Kaminski, "Tomographic absorption spectroscopy for the study of gas dynamics and reactive flows," *Prog. Energy Comb. Sci.*, **59**, pp. 1-31, 2017.

[33]   A.R. Piper, L.A. Todd and K. Mottus, "A field study using open-path FTIR spectroscopy to measure and map air emissions from volume sources," *Field Anal. Chem. Technol.*, **3**.2, pp. 69-79, 1999.

[34]   L.A. Todd, M. Ramanathan, K. Mottus, R. Katz, A. Dodson and G. Mihlan, "Measuring chemical emissions using open-path Fourier transform infrared (OP-FTIR) spectroscopy and computer-assisted tomography," *Atmos. Env.*, **35**.11, pp. 1937-1947, 2001.

[35]   T. Laepple, V. Knab, K.U. Mettendorf, and I. Pundt, "Longpath DOAS tomography on a motorway exhaust gas plume: numerical studies and application to data from the BAB II campaign," *Atmos. Chem. Phys.*, **4**.5, pp. 1323-1342, 2004.

[36]   M. Johansson, B. Galle, C. Rivera and Y. Zhang, "Tomographic reconstruction of gas plumes using scanning DOAS," *Bull. Volcanol.*, **71**.10, pp. 1169-1178, 2009.

[37]   G.G. Salerno, M.R. Burton, C. Oppenheimer, T. Caltabiano, D. Randazzo, N. Bruno and V. Longo, "Three-years of SO_2 flux measurements of Mt. Etna using an automated UV scanner array: comparison with conventional traverses and uncertainties in flux retrieval," *J. Volcanol. Geotherm. Res.*, **183**.1, pp. 76-83, 2009.

[38]   C. Rivera, J.A. García, B. Galle, L. Alonso, Y. Zhang, M. Johansson, M. Matabuena and G. Gangoiti, "Validation of optical remote sensing measurement strategies applied to industrial gas emissions," *Int. J. Remote Sens.*, **30**.12, pp. 3191-3204, 2009.

[39]   S. Zhang, J. Wang, D. Dong, W. Zheng and X. Zhao, "Mapping of methane spatial distribution around biogas plant with an open-path tunable diode absorption spectroscopy scanning system," *Opt. Eng.*, **52**.2, p. 026203, 2013.

[40]   C. Richard, I. E. Gordon, L. S. Rothman, M. Abel, L. Frommhold, M. Gustafsson, J. M. Hartmann, C. Hermans, W. J. Lafferty, G. S. Orton and K. M. Smith, "New section of the HITRAN database: Collision-induced absorption (CIA)," *J. Quant. Spectrosc. Radiat. Transfer*, **113**.11, pp. 1276-1285, 2012.

[41]   T. J. Johnson, R. L. Sams and S. W. Sharpe, "The PNNL quantitative infrared database for gas-phase sensing: a spectral library for environmental, hazmat, and public safety standoff detection," *Opt. Technol. Ind. Env. Biol. Sens.*, pp. 159-167, 2004.

[42]   K.E. Bennett and R.L. Byer, "Fan-beam-tomography noise theory," *JOSA A*, **3**.5, pp. 624-633, 1986.

[43]   L. Mandel and E. Wolf, *Optical coherence and quantum optics*. Cambridge, UK: Cambridge University Press. 1995.

[44]   S.R. Arridge and J.C. Schotland, "Optical tomography: forward and inverse problems," *Inv. Prob.*, **25**.12, p. 123010, 2009.

[45]   S.B. Pope, *Turbulent flows*. Cambridge, UK: Cambridge University Press, 2011

[46]   S.J. Grauer, P.J. Hadwin and K.J. Daun, "Improving chemical species tomography of turbulent flows using covariance estimation," *Appl. Opt.*, **56**.18, pp. x-x, 2017.

[47]   J. Shore and R. Johnson "Axiomatic derivation of the principle of maximum entropy and the principle of minimum cross-entropy," *IEEE Trans. Inf. Theory*, **26**.1, pp. 26-37, 1980.

[48]   K.J. Daun "Infrared species limited data tomography through Tikhonov reconstruction," *JQSRT*, **111**.1, pp. 105-115, 2010.

[49]   K.G.T. Hollands, *Thermal Radiation Fundamentals*. New York, NY: Begell House, 2004.

[50]   R.A. Hashmonay and M.G. Yost, "Localizing gaseous fugitive emission sources by combining real-time optical remote sensing and wind data." *J. Air Waste Manag. Assoc.*, **49**.11, pp. 1374-1379, 1999.

[51]   R.A. Hashmonay, D.F. Natschke, K. Wagoner, D. B. Harris, E. L. Thompson and M. G. Yost, "Field evaluation of a method for estimating gaseous fluxes from area sources using open-path Fourier transform infrared," *Env. Sci. Technol.*, **35**.11, pp. 2309-2313, 2001.

[52]   S.J. Grauer, P.J. Hadwin and K.J. Daun, "Bayesian approach to the design of chemical species tomography experiments," *Appl. Opt.*, **55**.21, pp. 5772-5782, 2016.

Highlights

- A broadband measurement model is developed for chemical species tomography.
- Transfer functions map broadband transmittances to a path-integrated concentration.
- A system of open-path broadband infrared detectors was constructed and calibrated.
- Target gasses in this study are methane, ethylene, and propane.
- The first broadband CST experiment is reported, featuring a propane plume source.